

Statistical dynamics of spatial-order generation by secrete-and-sense cells

Eduardo P. Olimpio^{a,b} and Hyun Youk^{a,b,1}

^aKavli Institute of Nanoscience,

^bDepartments of Applied Physics and Bionanoscience, Delft University of Technology,
Delft 2629HZ, the Netherlands

¹Correspondence to: h.youk@tudelft.nl

Classification:

Biological Sciences / Biophysics and Computational Biology

Keywords:

Secrete-and-sense cells | Cell-cell communication | Collective behaviours | Gene-expression coordination | Hamiltonian | Spatial order

Abstract

In multicellular systems, including microbial communities and developing organs, cells often communicate to coordinate their gene expressions and generate ordered spatial patterns or structures. ‘Secrete-and-sense cells’ simultaneously secrete and sense the same molecule. Their ubiquity in spatial order-forming systems and studies of specific secrete-and-sense cells suggest that they are ideal for spatially coordinating gene expressions. But whether secrete-and-sense cells from different organisms use shared principles to do so and how, in general, secrete-and-sense cells with initially uncorrelated gene expressions can dynamically establish spatially correlated gene expressions remain unclear. To address these questions, we developed a statistical mechanics-type framework for a simple class of secrete-and-sense cells. We consider slowly responding, bistable secrete-and-sense cells that turn on and off each other's ‘output gene’ expression and signal-secretions. We map an ensemble of cellular lattices with the same ‘macrostate’ variables – spatial order parameter and average output-gene expression – onto a particle that drifts and diffuses down a pseudo-energy landscape in a phase space defined by the macrostate variables. Decreasing pseudo-energy increases cells’ spatial order. Competing domains of on- and off-cells drive the particle’s drift. A Hamiltonian for cellular communication – analogous to that of magnetic spins with long-range interactions – determines the pseudo-energy landscape. Particles can be trapped outside their pseudo-energy’s minima, yielding metastable spatial patterns. Noise in secretion and sensing can liberate the trapped particles and further increase cells’ spatial order. We generalize our framework to multiple types of cells and signals. Our approach may be extended to understand more complex forms of cell-cell communications.

(250 words)

Significance statement

The adage that cells defy the tendency of matter to become more disordered over time partly stems from observing multicellular systems, such as microbial communities and developing organs, whose cells communicate to generate spatially ordered structures or patterns from disordered beginnings. Wide-spread examples are ‘secrete-and-sense cells’, such as quorum-sensing microbes and autocrine-signalling metazoan cells, that secrete and sense the same molecule. Why are they good at spatially coordinating gene expressions and what principles drive them? Inspired by statistical-physics approaches, we addressed these questions by grouping lattices of secrete-and-sense cells into an ensemble that moves as a particle in an abstract space with an underlying Hamiltonian for cellular communication. Our approach may inform quantitative frameworks for other forms of cell-cell communication.

(120 words)

Cells often communicate by secreting signalling molecules and this underlies their many collective behaviours. A striking example is cells, whose gene-expression levels are initially uncorrelated, using cell-cell communication to gradually coordinate their gene-expression levels over time and space such that they generate highly ordered spatial patterns or structures (1-4). Many cells that exhibit such disorder-to-order dynamics either partly or completely control their coordination of gene expressions by simultaneously secreting and sensing the same molecule (5, 6). Despite appearing in diverse organisms – including the quorum-sensing social amoeba *Dictyostelium* that form highly organized fruiting bodies (1, 7, 8) and autocrine-signalling T-cells (9, 10) – many of these ‘secrete-and-sense cells’, when stripped down to their basics, use the same genetic-circuit motif – the ‘secrete-and-sense circuit’ (Fig. S1A) (6) – to control their secretion of the signal, sensing of the signal, and one or more ‘output genes’ whose expression levels depend on the concentration of the extracellular signal (5)1. The ubiquity of the secrete-and-sense circuit (6), our previous theoretical analysis (11), and studies of specific examples of secrete-and-sense cells (1-5, 8, 12-22) suggest that secreting-and-sensing the same molecule is highly advantageous for cells in spatially coordinating their gene expressions, which is a basis for forming spatial patterns. But exactly why this is so, what the dynamics underlying the cells’ spatial order-generation is, and how to even quantify the cells’ spatial order in the first place, remain open questions for which we do not yet have answers that are common to numerous organisms. A common set of mechanisms may indeed address these questions for secrete-and-sense cells from various organisms given that the common secrete-and-sense circuit motif controls many of them (6). We sought to address these questions in the context of an initially disordered field of secrete-and-sense cells (i.e., the expression levels of the cells’ output genes are spatially uncorrelated) self-organizing into a more spatially ordered field (i.e., the expression levels of the cells’ output genes become more spatially correlated) without the aid of any pre-existing morphogens.

We sought to develop a theoretical framework that takes a simplified secrete-and-sense circuit, sensibly defines and quantifies the notion of spatial order for cells with this circuit, and then elucidates how the spatial order develops over time through analytical methods instead of brute-force numerical simulations. Our focus here is on asking if there is a generic metric and a theory for describing a spatial coordination of gene expression in a field of secrete-and-sense cells, which is a property that statistical measures such as spatial-correlation coefficients may characterize. By focusing on this underexplored issue for secrete-and-sense cells, our aim is different from describing the shape, size, and formation of a specific spatial pattern such as a stripe or an island. While exhaustive numerical simulations typically reveal how particular spatial

patterns arise and these studies yield valuable insights and testable results that are tailored to specific patterns or organisms (23-26), it would also be beneficial to formulate a conceptual picture of these complex processes from which one can analytically extract general principles that govern spatial coordination of gene expressions. The often-large numbers of parameters in numerical simulations that are adapted to particular systems and patterns have hindered formulating such a conceptual, yet still a practical model that applies to secrete-and-sense cells from various organisms. A complementary approach - one that we undertook – in which one uses abstractions to formulate a theoretical model would miss the full complexities of particular organisms and have a different focus than describing in detail the nature of specific patterns. But it may still provide basic principles that drive the dynamics of spatial coordination of gene expression by secrete-and-sense cells whose full gene-circuits can be constructed by adding more complex elements to the barebones secrete-and-sense circuit that we study here. The theoretical model may also serve as a springboard for more detailed modelling of particular secrete-and-sense cells and specific spatial patterns. Such has been the case for the cellular Potts model for describing mechanical shuffling of cells in tissues (27), the Vicsek model for studying collective motions of birds (28, 29), and theoretical approaches for studying spatial patterning driven by pre-existing (i.e., maternally deposited) morphogens (30-35). Motivated by these considerations, we sought principles that explain how and why a field of simple secrete-and-sense cells can self-organize spatial order over time by developing a theoretical framework.

As a proof-of-principle, we selected as a testbed a class of simple secrete-and-sense cells, namely cells that slowly respond to their fast diffusing signal and whose output-gene expression is sharply bistable in a switch-like manner (i.e., ON or OFF) due to a strong positive feedback, which the sensed signal controls, that toggles between two values their output-gene expression level (ON/OFF) and signal-secretion rate (high/low) (Fig. S1B-C) (5). To test our theory, we simulated the cells' gene-expression dynamics – first deterministically and then with stochastic effects – with a cellular automaton whose rules were inspired by experimentally observed behaviours of such cells. Our main idea is while predicting the exact evolution of even these simplified cells' spatial patterns over time without running full numerical simulations (i.e., the cellular automata) is infeasible, we can analytically determine how an ensemble of spatial patterns that have the same spatial order, which we will quantify, evolves over time. Here, we were inspired by the statistical-physics approach of drawing systems-level conclusions with limited information about each constituent particle. Likewise, we will group different spatial patterns into an ensemble, which we call a 'macrostate', if they have the same two macrostate variables: a 'spatial order parameter', which is a number between zero (complete disorder) and

one (complete order), and an average output-gene expression level per cell. Both are measurable in experiments. Our main results will be that these two macrostate variables denote positions in an abstract space ('phase space') and that an ensemble of spatial patterns moves through this space, undergoing changes in its spatial order and average output-gene expression over time, like a drifting-and-diffusing particle with a precise equation of motion. We will show that our ignorance of the exact 'microstate' (i.e., not knowing every cell's output-gene expression level due to the macrostate-approach) is responsible for the particle's diffusion and that competitions among expanding domains of ON- and OFF-cells in the lattice cause the particle's drift towards regions of higher spatial order in the phase space. Crucially, this drift pushes the particle down a 'pseudo-energy' landscape whose shape is defined by a 'Hamiltonian' for cell-cell communication, which we define, that resembles the Hamiltonians of magnetic spins with long-range spin-spin interactions and an external magnetic field. We will show that the particles can be trapped at sloped regions of the pseudo-energy landscape and that this causes metastable spatial patterns that are highly ordered especially when the cell-cell communication is strong. Finally, we demonstrate how to extend our framework to cells that stochastically secrete and sense as well as to lattices with arbitrary numbers of cell-types and signal-types (e.g., paracrine signalling). We will end by proposing how to use our framework in experiments. Throughout, we indicate relevant sections and figures in the Supporting Information (SI) that provide full derivations and more in-depth discussions of the main results.

Results

Experimentally motivated cellular automaton for simple secrete-and-sense cells. We considered a two-dimensional triangular lattice of N identical, spherical, and immobile secrete-and-sense cells of radius R and a lattice spacing a_0 (Fig. S1; SI section 1.1). We chose triangular lattices because they are ubiquitous in tissues and organs (Table S1). We used cellular automaton (36) to simulate secrete-and-sense cells whose exact results will be compared with our theory. We consider 'simple' secrete-and-sense cells that 1.) very slowly respond to their fast diffusing signal, and 2.) whose output-gene expression level and signal-secretion rates exhibit switch-like bistability (Fig. S1). These two features were motivated by experimentally characterized, immobile secrete-and-sense systems. Examples of very slowly responding systems with a very fast diffusing signal include budding yeasts that secrete-and-sense a mating pheromone (diffusion timescale ~ 1 s; response timescale ~ 30 minutes) (5, 37) and mouse hair follicles, which are secrete-and-sense organs that have been shown to act as point-like secrete-and-sense cells on a triangular lattice (diffusion timescale ~ 12 hours;

response timescale ~ 1.5 days) (38). Numerous secrete-and-sense cells' output-gene expression and signal-secretion rate are bistable (5, 6) because the secrete-and-sense circuit consists of 1.) a positive feedback that controls the signal-secretion rate and the output-gene expression (i.e., increasing the concentration of the sensed signal increases the signal secretion rate), and 2.) a negative feedback that additionally controls the signal-secretion rate or a secreted protease that degrades the signal via first order chemical kinetics. Analogous to the intracellular gene-circuits that are bistable such as the galactose network in yeast (39, 40), tuning these two elements give rise to bistable secrete-and-sense cells (5). In some cases, the Hill coefficient for the positive feedback is sufficiently high (e.g., equal to two) such that the secrete-and-sense cell nearly acts as a digital switch (5) as in our model. Examples of secrete-and-sense systems with bistable responses include yeasts that secrete-and-sense the mating pheromone – these yeasts have a nearly digital secretion and output-gene expression due a Hill coefficient of two (5) – T-cells that secrete-and-sense IL-2 (12), and mouse hair follicles (38). In our model, each cell senses the steady-state signal-concentration c on itself. This sets the cell's signal-secretion rate (high or low) and its output-gene expression level (ON or OFF). If the c on the cell is larger (lower) than a threshold concentration K , then the cell is ON (OFF). The ON-cell secretes the signal at a constant rate such that a lone ON-cell (i.e., $N=1$) would maintain a concentration C_{ON} on itself whereas a lone OFF-cell would maintain a concentration of 1 on itself (where $C_{ON} > 1$). With these rules, the cellular automaton proceeds by computing the steady-state value of c on every cell, then updating each cell's state as determined by the c on each cell, and then repeating this process until we reach a steady-state, in which no cell's state requires further updates (SI section 1.1). We previously found that in this cellular automaton, an initially disordered secrete-and-sense cells can morph into highly ordered steady-state spatial patterns such as islands of ON-cells (Fig. 1A) (11). We sought principles that drive these dynamics.

Behavioural phases of secrete-and-sense cells. Our task is to analyse the cellular automaton for each of the distinct 'behavioural phases' of secrete-and-sense cells (Fig. 1B). These phases, which our previous work classified (11), represent how one cell turns on/off another cell. They arise from a competition between self-communication (cell secretes a molecule and captures it right back) and neighbour-communication (cell sends its molecule to the other cells, including cells that are beyond the nearest neighbours) (Fig. S1A). This competition is tuned by the values of K , C_{ON} , and an 'interaction strength' that characterizes the strength of neighbour-

communication, $f_M(a_o) = \sum_{j \neq i} \frac{e^{R-r_{ij}}}{r_{ij}} \sinh(R)$, where r_{ij} is the distance between cell- i and cell- j that is a multiple of a_o (11). Since these three values are held fixed from start to finish of a cellular automaton, the cells' behavioural phase is held fixed in each run of the cellular automaton. As described in our previous work (summarized in SI sections 1.2-1.3) (11), any behavioural phase is either an 'insulating phase' or a 'conducting phase'. In the insulating phases, no cell can turn on/off the other cells because each cell is inert to the other cells' signals (due to dominant self-communication). In the conducting phases, cells can turn on/off the other cells (due to dominant neighbour-communication) (Fig. 1B and Fig. S2). When the interaction is weak (i.e., $f_M(a_o) < 1$), the cellular automaton can operate in the 'autonomy phase' – this an insulating phase in which each cell, due to its self-interaction, can autonomously stay ON or OFF regardless of the other cells' states. A weak interaction ($f_M(a_o) < 1$) also allows the cells to operate in conducting phases such as the 'activate phase' – a phase in which enough neighbouring ON-cells can turn on an OFF-cell – and the 'deactivate phase' – a phase in which enough neighbouring OFF-cells can turn off an ON-cell (SI section 1.2 quantifies what is 'enough'). The critical interaction strength (i.e., $f_M(a_o) = 1$) is the lowest interaction strength for which cells can no longer be autonomous (Fig. 1B; Fig. S2). When the interaction is strong (i.e., $f_M(a_o) > 1$), the cells can operate in the 'activate-deactivate phase' in which they can both activate and deactivate each other depending on their relative locations (Fig. 1B). This yields some of the most highly ordered steady-state configurations such as islands and stripes of ON-cells (11).

Macrostate variables. We sought to quantify the cells' spatial order and then explain how it evolves for each behavioural phase. To do so, we first group the 2^N possible spatial configurations into 'macrostates'. A macrostate represents an ensemble of spatial configurations that have the same two quantities (Fig. 2A) – a fraction p of cells that are ON ($0 \leq p \leq 1$), and a 'spatial order parameter' I defined as

$$I = \frac{N}{\sum_i \sum_{j \neq i} f(r_{ij})} \frac{\sum_i \sum_{j \neq i} f(r_{ij})(X_i - \langle X \rangle)(X_j - \langle X \rangle)}{\sum_i (X_i - \langle X \rangle)^2} \quad [1]$$

where $f(r_{ij}) = \frac{e^{R-r_{ij}}}{r_{ij}} \sinh(R)$ is the interaction term for the cell-pair i - j , and X_i is +1 for an ON-cell and -1 for an OFF-cell (see examples of spatial configurations and their I in Fig. 2A and Fig. S3). Roughly speaking, the spatial order parameter is a number that represents the average correlation between any two cells in a lattice whereby each cell-pair's correlation is weighted by the communication strength of that pair (SI section 2.1) (11, 41). The magnitude of the spatial order parameter $|I|$ is always between zero and one. As $|I|$ approaches 0, the spatial

configuration becomes more disordered. As $|I|$ approaches 1, the spatial configuration becomes more ordered (Fig. 2A; Fig. S3). At precisely $I=0$, ON- and OFF-cells are randomly distributed, resulting in a maximally disordered lattice. The p also represents the average output-gene expression level per cell. With the p and the I as macrostate variables, our main idea is that we view a cellular lattice as a particle that moves in an abstract space ('phase space') whose position is (p, I) . Each point in this p - I space represents a particular macrostate – an ensemble of potentially thousands of spatial configurations ('microstates') with the same values for p and I . We sought to determine an equation of motion for the particles – that is, find $(p(t), I(t))$ as a function of time t – as they move from an initially disordered configuration $(p_{\text{initial}}, 0)$ to a steady-state configuration $(p(t_{\text{final}}), I(t_{\text{final}}))$ after time t_{final} .

Properties of particle trajectories. To learn how the particles move, for each starting position $(p_{\text{initial}}, 0)$, we randomly chose thousands of microstates that have the same value of p_{initial} and then ran the cellular automaton for each (SI section 2.2). This gave us a distribution of their final positions (i.e., $p(t_{\text{final}})$) for each value of p_{initial} and each behavioural phase (Fig. 2B-C – left columns). The fact that we obtained a distribution of values for each starting position, rather than a single value, indicates the stochastic nature of the particles that stems from the automaton caring about the microstates rather than the macrostates (i.e., the automaton operates on individual cells and not on the macrostate variables, p and I). Likewise, we obtained an ensemble of trajectories $(p(t), I(t))$ for each starting position, rather than a single trajectory (Fig. 2B – right column; Figs. S4-S6). Intriguingly, we found that the thousands of particles that started from the same position $(p_{\text{initial}}, 0)$, for the most part, remained close to each other over time, yielding tightly bundled trajectories (Fig. 2B – right column). This did not have to be the case because no information about the macrostates explicitly entered into the cellular automaton's rules. From observing the trajectories, we learned their basic behaviours. In every trajectory, we found that the spatial order initially increased before it plateaued while the p either increased or decreased over time (Fig. 2B – all trajectories). Then, one of two events occurred. Either 1.) the particle stops moving before its p reaches an extreme value (i.e., zero or one) (examples in Fig. 2B – green trajectories in 'activate-deactivate phase'); or 2.) the particle reaches an extreme value of p and as it does so, the spatial order sharply and suddenly decreased to zero (examples in Fig. 2B – red trajectories in 'activate phase'). We next sought an equation of motion that recapitulates these features.

Drifting-and-diffusing particles represent cellular lattices. To explain the observed

trajectories, we first rewrite Eq. 1 as

$$I = \frac{\langle \sum_{j \neq i} f(r_{ij}) X_i X_j \rangle_i - (2p - 1)^2 f_N(a_o)}{4p(1 - p) f_N(a_o)} \quad [2]$$

to examine how the spatial order depends on the p . Eq. 2 shows that for each value of p , there is a maximally allowed value for the spatial order due to a finite number of ways of arranging a fixed number of ON-cells. In fact, when the p is in a close vicinity of zero or one, the maximal spatial order $|I|$ sharply drops to zero and thus the spatial order of any particle must also drop to zero (SI section 2.1), as we indeed noted above. But this does not mean that the cells are becoming more uncoordinated. On the contrary, the cells' output-gene expressions are becoming more correlated, with either all cells becoming ON (i.e., $p=1$) or all cells becoming OFF (i.e., $p=0$). Thus, care must be taken to interpret the spatial order when all cells are becoming ON or OFF. For this reason, we define a 'normalized spatial order', $\Theta = \langle \sum_{j \neq i} f(r_{ij}) X_i X_j \rangle_i$, which appears in Eq. 2 and sought an equation of motion in terms of it. The normalized spatial order always increases as the cells become more correlated, including when the cells are all turning ON or OFF. It measures the average correlation between two cells that is weighted by the strength of communication between them (i.e., $f(r_{ij})$), with a higher weight placed if there is a stronger cell-cell communication. It discounts fortuitous correlations between cells that result from little or no communication. We hypothesized that we can explain the stochastic nature of the particle trajectories by a drift-diffusion process (42). Our idea is that the particle drifts towards higher spatial orders, as we indeed noted above, due to a yet-to-identified mechanism while our ignorance of the precise microstate at any given time yields the diffusive (stochastic) motion. In terms of p and Θ , we thus conjectured that

$$\begin{cases} p(t + 1) = p(t) + \Delta p(t) > +\eta_{\Delta p} \\ \Theta(t + 1) = \Theta(t) + \Delta \Theta(t) > +\eta_{\Delta \Theta} \end{cases} \quad [3]$$

where $\Delta p(t) \equiv \langle p(t + 1) - p(t) \rangle$, $\Delta \Theta(t) \equiv \langle \Theta(t + 1) - \Theta(t) \rangle$, $\eta_{\Delta p}$ is the noise in Δp , and $\eta_{\Delta \Theta}$ is the noise in $\Delta \Theta$. The noise terms represent our ignorance the microstates rather than biological noise (we will investigate biological noise below). The $p(t)$ and the $\Theta(t)$ uniquely specify $I(t)$ (SI section 2.4). By determining how many cells are likely turn on and how many cells are likely turn off in each time step (SI section 2.3), we analytically determined the means, the variances, and statistical properties of $\Delta p(t)$ and $\Delta \Theta(t)$ (SI section 2.4). Combining these analytical estimates with Eq. 3 completely specifies the particle's stochastic trajectories – $(p(t), \Delta \Theta(t))$ (SI section 2.5). To check our estimates, we compared the particle trajectories from the cellular automata with those dictated by the equation of motion (Eq. 3). For this, we need to visualize the stochastic trajectories produced by Eq. 3. Thus we ran Monte Carlo

simulations of Eq. 3 based on an algorithm that we developed – a ‘branching algorithm’ – that is similar to the ‘pruning algorithm’ for simulating two-player games and protein folding (see Methods; SI sections 2.3 and 2.5; Figs. S7-S8) (43). From the comparisons, we found that the equation of motion closely estimated where the particles stopped (e.g., distribution of values of $p(t_{\text{final}})$ for each value of p_{initial}) (Fig. 2C) as well as the average time $\langle t_{\text{final}} \rangle$ taken by the secrete-and-sense cells to form steady-state configurations (Fig. 2D) (Figs. S9-S13). The equation of motion (Eq. 3) thus recapitulates some of the main features of the particle’s motion.

Mechanism that drives spatial ordering. We next sought a mechanism that causes the particle’s drift towards higher spatial orders. For this, we adapted a technique for analysing the 2D Ising model’s critical phenomena in which polygons enclose islands of ON-cells (Fig. 3A) (42). By coupling this with a mean-field approach that determines how the polygonal islands expand and shrink (see Methods), starting from randomly distributed ON- and OFF-cells, we discovered that the cells’ normalized spatial order Θ monotonically increases and that this is driven by the islands of ON- and OFF-cells competing for growth (SI sections 3.1-3.2). In brief, analysing the polygonal islands led us to estimate the spatial order (SI section 3.2) as

$$I(t) \approx \frac{(\langle m_{ON}(t) \rangle - 6p(t))f(a_o)}{(1 - p(t))f_N(a_o)} \quad [4]$$

where $\langle m_{ON} \rangle$ is the average number of ON nearest neighbours of any cell. This estimate closely agrees with the exact value of the spatial order $I(t)$ obtained from the cellular automata (example shown in Fig. 3B) and is rooted in the fact that for an island to grow, some other island has to shrink due to the finite total area. Furthermore, we could deduce that the $\langle m_{ON} \rangle$ and the total area of all the polygons monotonically increase over time, again by analysing the competing islands (Figs. S14-S16). Combining these facts with Eq. 4 leads to the conclusion that the normalized spatial order Θ and the spatial order I monotonically increase over time (with the caveat for I at the extreme values of p) (SI section 3.2). Eq. 4 also lets us deduce a maximally allowed spatial order, I_{max} , for each value of p (Figs. 3C and 3D (black curves); SI section 3.2), that closely matches the actual maxima that the particles reach (Fig. 3D – red curves).

Hamiltonian for cellular communication. A missing mechanism so far is one that steers the left-right motion of the particle (i.e., a mechanism that determines whether the p increases or decreases). For example, in the activate phase, some values of p_{initial} cause more cells to turn on over time while for others, p does not change (Fig. 2C). Motivated by the particle picture, we

wondered if there may be a ‘landscape’ on which the particle rolls downwards. This may naturally determine whether more cells turn on or off over time. We define a function H , which we call a ‘multicellular Hamiltonian’,

$$H = - \sum_i X_i (Y_i - K) \quad [5]$$

where Y_i is the signal concentration on cell- i . Remarkably, the H is in fact a function only of p and l , and thus plotting $h(p, l) = H(p, l)/N$ in the p - l space yields a landscape that we call a ‘pseudo-energy landscape’ (Fig. 3C; SI section 3.3). The landscape’s shape depends on the cells’ behavioural phase (Fig. 3D). Importantly, by tracking each particle’s trajectory on the landscape (i.e., $h(p(t), l(t))$), we found that the particle’s pseudo-energy decreases over time until it halts (see Methods; mathematical proof in SI section 3.3). For example, plotting the particles’ trajectories (e.g., those in Fig. 2B) on top of their respective pseudo-energy landscapes shows that the particles drift and diffuse down their landscapes until they halt (Fig. 3D). The location of the pseudo-energy landscape’s peak, which occurs at $l=0$ for all three conducting phases (Fig. 3D), determines for which values of p_{initial} the particle’s p increases in subsequent times. Thus indeed the landscape provides a nature mechanism for steering the particle’s left-right motion. Aside from the particle picture, we realized another physical analogy by rewriting the H as

$$H = - \frac{C_{ON} - 1}{2} \sum_i \sum_{j \neq i} f(r_{ij}) X_i X_j - B \sum_i X_i - \frac{N(C_{ON} - 1)}{2} \quad [6]$$

where B is a ‘signal field’ identified as $\left(\frac{C_{ON}+1}{2}\right)(1 + f_N(a_o)) - K$. Eq. 6 is strikingly similar to the Hamiltonian of the Hopfield network (44, 45) and magnetic spins with long-range interactions (long-range interactions are typical in spin glasses (46, 47)) which is,

$$\mathcal{H}(\sigma) = \sum_{(i,j)} J_{ij} \sigma_i \sigma_j - B_o \sum_i \sigma_i \quad [7]$$

where B_o is an external magnetic field, σ_i and σ_j are spin- or neuron-states, and J_{ij} is the interaction strength for the spin- or neuronal-pair i - j (44-47). Intriguingly, researchers have previously noted that certain intracellular gene-networks could be mapped to spin systems (48). This may be combined with the mapping of our multicellular network to spins in order to analyze secrete-and-sense cells with more complex gene-networks in the future. But unlike the Hopfield network and spin glasses, the pseudo-energy landscape has no local minima in the p - l -space that can trap particles. The pseudo-energy landscape does not behave like a physical-energy landscape because, as we noted before, it can trap particles at its sloped regions (i.e., at

intermediate values of p , where p is neither zero nor one). This trapping is particularly evident in the activate-deactivate phase (Fig. 3D – blue curves; Fig. 3E – brown curves). Nonetheless, the analogy to spins is useful. The signal field is a knob that one can tune in experiments (via the circuit parameters and lattice spacing) to sculpt the pseudo-energy landscape (Fig. 3F). It competes with the cell-cell interaction term (with coupling constant $-\frac{c_{ON}-1}{2}f(r_{ij})$) just as the magnetic field does in spin systems and Hopfield networks: A positive B corresponds to the activate phase, a negative B corresponds to the deactivate phase, and a zero B corresponds to the activate-deactivate phase (Fig. 3F; Fig. S17; SI section 3.3).

Trapping configurations are akin to frustrations. ‘Trapping configurations’, which are steady-state spatial configurations with intermediate values of p , arise from the fact that 1.) the particle can only change its p and l in discrete step sizes and that 2.) the l depends on p . In other words, the trapping configurations represent trapped particles that do not have any accessible paths to decrease their pseudo-energies further to reach the either extremes of p , which would minimize their pseudo-energies. The situation here is similar in flavour to, but not the same as, the notion of frustration in spin systems. As an example, consider the configuration of cells in Fig. 3A which are in the activate-deactivate phase. Here, one can show that for an OFF-cell to turn on, at least three of its nearest neighbours must be on whereas for an ON-cell to turn off, at least five of its nearest neighbours must be on. Since the lattice is triangular, neither of the two conditions can be met even though both would decrease the pseudo-energy. This represents a particle trapped due to geometric restriction placed by the cells’ spatial arrangement. In fact, we determined the total number of steady-state configurations, and thus in turn the trapping configurations, for every interaction strength and behavioural phase (SI section 3.4). We found that the trapping configurations are most abundant in the activate-deactivate phase (for strong interactions) and in the autonomy phase (for weak interactions) (Fig. S18). As we will show below, in the presence of biological noise, the trapping configurations still exist but noise can push a particle from one trapping configuration to a different trapping configuration.

We have now presented the main elements our framework. In the next two sections, we demonstrate how to extend it to account for stochastic gene expression (49-59) and lattices with multiple cell-types and signal-types.

Extension to noisy secretion and sensing. We have so far considered deterministic gene expressions. But due to stochastic nature of gene expressions (52), the secretion rate and the threshold K , for example, would vary in real cells. As a proof-of-principle, we focused on letting

only the threshold fluctuate from cell to cell. In each time step of the automaton, we now pick a new value of the threshold $K + \delta K$ for each cell, where the K is the same for all cells and δK is a normally distributed noise with a mean of zero and a variance of α^2 (Fig. 4A; SI section 4.1). We define a noise strength, $\xi = \alpha/K$ and calculated the minimum noise strength ξ_{min} required to drive the steady states of the deterministic automaton out of their equilibrium (Fig. S19; SI section 4.2). Specifically, introducing a low noise ($\xi < \xi_{min}$) cannot push a trapped particle out (Fig. 4B – left column) while a high noise ($\xi > \xi_{min}$) kicks the trapped particle out and rolls it further down the landscape to regions that were inaccessible prior to the noise, increases its normalized spatial order, and eventually causes everyone to turn off or on (Fig. 4B – right column; Fig. S20; SI sections 4.3-4.4). Finally, introducing a moderate noise ($\xi \sim \xi_{min}$) drives the trapped particle to a new trapping configuration with an intermediate value of p . In this sense, the trapping configurations are metastable configurations. They are particularly abundant in the activate-deactivate phase (Fig. S18), many of which, we observed, exhibited very slow dynamics that are reminiscent of glassy dynamics – their p , l , and h changed so slowly that over hundreds of time steps, the spatial configuration essentially remained the same (Fig. 4C). As real tissues need to maintain stable spatial patterns in presence of fluctuations in their gene expressions, this observation is of interest and would require further studies to fully understand its origins. The activate-deactivate phase also special because a moderate noise substantially increases the maximal spatial order l_{max} that the cells can have (Fig. 4D; Fig. S21; SI section 4.5). The equation of motion (Eq. 3) could be extended to include the noisy sensing (SI section 4.5) and recapitulate the main features for the noisy cells (Fig. 4E and Figs. S22-S23).

Extension to multiple cell types. As our final step, we show how to extend our framework to lattices consisting of an arbitrary numbers of cell types and signals. In particular, we now allow for paracrine-signalling as well as secreting-and-sensing (Fig. 5A). Paracrine signaling involves two cells, where one secretes but cannot sense a signal while the other cell senses but cannot secrete the signal (6). Paracrine signalling and secreting-and-sensing account for the vast majority of cellular communications that involve diffusing signals (60). We consider a lattice composed of an arbitrary number of cell-types and signals (Fig. 5B). Each cell-type u has its own parameters (K_u , $C_{ON,u}$, and $C_{OFF,u}$) that are analogous to the parameters have been using so far. We now generalize the interaction strength $f_N(a_o)$ to an interaction-strength matrix F that quantifies how a cell-type m interacts with a cell-type n (examples in Fig. 5B; SI section 5.1). We can extend the multicellular Hamiltonian H to a lattice with L cell-types:

$$H = - \sum_{u=1}^L \left(N\theta_u + B_u \sum_{i \in u} X_i \right) \quad [8]$$

where θ_u is the normalized spatial order of cell-type u , and B_u is the signal field for cell-type u . We found this new Hamiltonian also monotonically decreases over time and that the normalized spatial order for each cell type monotonically increases over time (SI section 5.2). We also found that, as before, the signs of the signal fields determine how the p_u – the fraction of cells of type u that are ON – changes over time (examples in Fig. 5C; see Methods and SI section 5.2). Finally, when the signal field for every cell-type is zero – analogous to the activate-deactivate phase for a lattice composed of identical secrete-and-sense cells – we observed metastable trapping configurations of high spatial orders. While more detailed studies are needed, these observed properties suggest that the key results for single cell-type survive the extension to multiple cell-types.

Discussion

Here we proposed an explanation for why and how simple secrete-and-sense cells' gene expressions become more spatially organized over time in the absence of any pre-existing morphogens. This process is self-organized by the cellular lattice and is of interest to developmental systems such as the mouse and human embryos. Instead of focusing on understanding how specific spatial patterns such as stripes and islands emerge, we focused on the overall spatial order – a statistical measure of cell-cell coordination of gene expressions. This macrostate description has the advantage of making exhaustive numerical simulations unnecessary but has the disadvantage of being ignorant of the specific spatial patterns that form. The spatial order parameter, however, still allows us to describe what kinds of spatial patterns are formed because its value represents an ensemble of similar patterns (Fig. 2A; Fig. S3). With this approach, we have shown that domains of ON- and OFF-cells compete to expand and that this drives the spatial order to increase. We have also shown that a Hamiltonian underlies the cellular communication and that this defines a pseudo-energy landscape on which an abstract particle, representing the lattice of secrete-and-sense cells, drifts and diffuses downwards, increasing the cells' spatial order in the process and generating metastable spatial configurations.

As a proof-of-principle, we have used simple secrete-and-sense cells. The theory does not yet account for many complex forms of secrete-and-sense cells that we would obtain by relaxing the imposed constraints. An example is a secrete-and-sense cell with continuous values for its output-gene(s) expression level(s) and secretion rate, a low Hill coefficient for its

positive feedback that controls its secretion rate, and responding on a timescale that is similar to that of the signal-diffusion. Two such cells that are far apart may have difficulties in coordinating their gene expressions. Among others, this may lead to localized domains of orders, defined by the timescales for the signal-diffusion and the cell's response. It would be interesting to study these types of extensions in the future.

Experimentally, one can measure the two macrostate variables, p and l , in a microscope image (e.g., by tagging fluorescent protein(s) to the output gene(s)). Thus, our model and its extensions may be useful for understanding time-lapse movies of secrete-and-sense cells that generate spatial order. Along with studying how specific spatial patterns such as stripes and islands are generated, focusing on the statistical description of how certain 'types' of spatial order – representing cells' spatial coordination of their gene expressions – is useful because one often cannot measure all the parameters that are required for a detailed numerical modelling (e.g., gene-expression level of every cell in a tissue). In such situations, our framework and its extensions may help in predicting, based on a limited knowledge of the underlying gene-circuit and an estimate of the tissue's initial spatial order, what types of spatial order and patterns would likely emerge without revealing the exact location, shape, and size of the resulting pattern. In the polar opposite situation in which one can obtain detailed measurements of gene-expressions in every cell in tissues or embryos (61, 62) – a situation that is becoming increasingly common in recent years – one is often overwhelmed by the large volume of data and a conceptual picture that gives a systems-level description, rather than a description at the level of every individual cell, would be helpful (63). Here too, frameworks such as ours that describe statistical dynamics of multicellular systems in terms of macrostates may be of a practical value.

Methods

Number of steady-state spatial configurations and trapping configurations. A full derivation is in SI section 1.3. We treat the state of each of the N cells as a random variable, with the constraint that p is fixed. If we consider only the signal that a cell senses due to the secretion of all the other cells (i.e., excluding the signal secreted by the cell itself), its concentration Y_i^{others} obeys the following statistics

$$\mu_p \equiv \langle Y_i^{others} \rangle = [(C_{ON} - 1)p + 1]f_N(a_o) \quad [9a]$$

$$\sigma_p^2 \equiv \langle (Y_i^{others})^2 \rangle = (C_{ON} - 1)^2 p(1 - p)[f_N(a_o)]^2 \quad [9b]$$

where μ_n and σ_n^2 are mean and variance of Y_i^{others} respectively that are determined by averaging over all the $\binom{N}{n}$ spatial configurations that have n ON-cells. By assuming that the probability P_{ON-ON} that an ON-cell stays on and the probability $P_{OFF-OFF}$ that an OFF-cell stays off are normally distributed, it follows that μ_n and σ_n^2 specify the fraction of the $\binom{N}{n}$ spatial configurations that are steady states. Summing over all n yields an estimate for the total number of steady states. The total number Ω_E of steady state spatial configurations that a cellular lattice can have is the sum of the number Ω_p of steady state configurations for each value of p ,

$$\Omega_E = \sum_{n=0}^N \Omega_{p=n/N} = \sum_{n=0}^N \binom{N}{n} \left[1 - \text{erf} \left(\frac{K - C_{ON} - \mu_p}{\sqrt{2}\sigma_p} \right) \right]^n \left[1 + \text{erf} \left(\frac{K - 1 - \mu_p}{\sqrt{2}\sigma_p} \right) \right]^{N-n} \quad [10]$$

In the autonomy phase and the activate-deactivate phase, except for two configurations (one in which everyone is ON and one in which everyone is OFF), all of these steady state configurations are trapping configurations. In the other phases, almost all of the steady-state configurations have either $p=0$ (all cells are OFF) or $p=1$ (all cells are ON).

Transition matrix formalism. Full details are in SI section 2.3. Consider a randomly picked spatial configuration with n ON-cells. The transition matrix Ξ determines the probability that one spatial configuration becomes another spatial configuration after one time step, for any pairs of spatial configurations and yields a macrostate-level description. Specifically, its matrix element $\Xi_{n_f, n}$, is the probability that, if we randomly pick one out of the $\binom{N}{n}$ spatial configurations with n ON-cells, the selected spatial configuration will have n_f ON-cells in the next time step. Using the probabilities P_{ON-ON} and $P_{OFF-OFF}$ that we used to calculate the number of trapping configurations (SI section 1.3), we can calculate the probability that a cell will change its state, which is $P_{ON-OFF} = 1 - P_{ON-ON}$ for ON-cells and $P_{OFF-ON} = 1 - P_{OFF-OFF}$ for OFF-cells. We then use these to calculate the probability that y_+ cells will turn on and y_- cells will turn off in the next time step. Summing

the probabilities $p(y_+, y_-; n)$ for all possible pairs (y_+, y_-) , we obtain the transition probability $\Xi_{n_f, n}$.

Mean-field approximation. Full details are in the SI section 3.1 and SI Appendix A. With our periodic boundary condition (see SI section 1.1), the signal concentration $Y_i^{neighbour}$ on cell- i due to everyone else is $Y_i^{nearest} + Y_i^{distant}$, where $Y_i^{nearest}$ is due to its nearest neighbours and $Y_i^{distant}$ is due to all the other cells. For a mean-field approximation, we calculate $Y_i^{nearest}$ exactly by using the number m_{ON}^i of the nearest neighbours of cell- i that are ON and $Y_i^{distant}$. Using this mean-field approach, which ignores the precise location ON/OFF- cells other than those that are the nearest neighbours, we can compute p . Moreover, using this approach, we can show that the average number of ON-neighbours $\langle m_{ON} \rangle$ monotonically increases over time.

Langevin-type dynamics in the p - l space. Full details are in SI section 2.4. Eq. 3 describes the particle (cellular lattice) dynamics, in terms of the macrostate variables p and l , with the Langevin approach. This description requires calculating the drift and the noise for both p and θ . The probability that an ON-cell turn off in the next time step is $1 - P_{ON-ON}$. The probability that an OFF-cell turns on in the next time step is $1 - P_{OFF-OFF}$. Then if we assume that N is sufficiently large so that p assumed to be a continuous variable, we have

$$\langle \Delta p(t) \rangle = \sum_{n'=1}^N \left(\frac{n'}{N} - p(t) \right) \Xi_{n', n(t)} \approx (1 - p(t))(1 - P_{OFF-OFF}) - p(t)(1 - P_{ON-ON}) \quad [11]$$

Analogously, we can estimate the variance of the noise $\eta_{\Delta p}$ by assuming that the switching of the ON- and OFF-cells are independent of each other:

$$Var(\eta_{\Delta p}) = \frac{1}{N} [(1 - p(t))(1 - P_{OFF-OFF})P_{OFF-OFF} + p(t)(1 - P_{ON-ON})P_{ON-ON}] \quad [12]$$

For the normalized spatial order parameter θ , we can use its definition deduce that $\Delta \theta = 2\langle \sum_{j \neq i} f(r_{ij}) \Delta X_i X_j \rangle_i + \langle \sum_{j \neq i} f(r_{ij}) \Delta X_i \Delta X_j \rangle_i$ and then calculate the mean and the variance of both terms in this expression. We approximate the second term in the expression as $\langle \sum_{j \neq i} f(r_{ij}) \Delta X_i \Delta X_j \rangle_i \approx 4 f_N(a_o) (\Delta p)^2$ and use the mean and the variance calculated for Δp to proceed further. For the first term in the expression for $\Delta \theta$, we have

$$\langle \sum_{j \neq i} f(r_{ij}) \Delta X_i X_j \rangle_i \approx \frac{4y_+}{N} \langle \sum_{j \neq i} f(r_{ij}) X_j \mid i: OFF; Y_i > K \rangle_i - \frac{4y_-}{N} \langle \sum_{j \neq i} f(r_{ij}) X_j \mid i: ON; Y_i < K \rangle_i \quad [13]$$

Invoking the Central Limit Theorem, both averages in the above expression (averaged over all cells) can be thought of as truncated Gaussian distributions from which the mean and variance are calculated to determine $\langle \Delta\theta(t) \rangle$ and $Var(\eta_{\Delta\theta})$.

Proof that the multicellular Hamiltonian monotonically decreases over time. Full details are in SI section 3.3. Here we outline the proof. In the multicellular Hamiltonian (Eq. 6), we have three terms to consider. The third term is a constant. The first term monotonically decreases over time because $\langle m_{ON} \rangle$ monotonically increases over time, as we have shown with the mean-field approach (SI section 3.1). The second term in Eq. 6 is negative when $\sum_i \Delta X_i$ and B have opposite signs. For the secrete-and-sense cells that operate in the insulating phases, $\Delta X_i = 0$ and consequently $\Delta H = 0$. In the activate phase, we have $B > 0$ and in the deactivate phase, we have $B < 0$, implying that the second term decreases in those phases. In the activate-deactivate phase, there is activation when $B > 0$ and deactivation when $B < 0$ (Fig. S18). Putting everything together, we conclude that the multicellular Hamiltonian monotonically decreases over time.

Monte Carlo simulation of statistical dynamics based on equation of motion (Eq. 3). Full details are in SI section 2.5. We performed the Monte Carlo simulations of the drifting-and-diffusing particles with the Euler Method for stochastic differential equations. Based on the current macrostate $(p(t), \theta(t))$ (i.e., particle's current position), we calculate a drift $(\langle \Delta p(t) \rangle, \langle \Delta \theta(t) \rangle)$ and sample two random numbers using the Marsaglia polar method with variance $Var(\eta_{\Delta p})$ and $Var(\eta_{\Delta \theta})$ to calculate the subsequent macrostate $(p(t+1), \theta(t+1))$. This macrostate has a probability $P = P_{ON-ON}^n P_{OFF-OFF}^{N-n}$ of being a steady state. Therefore, we uniformly sample a number z between 0 and 1. If $z < P$, then we consider the spatial configuration to be in a steady state. Running this procedure several times, it is possible to realize many different particle trajectories, which we compare with those obtained by the cellular automaton (Figs. 2C-D).

Extension to multiple cell types with multiple signals. Full details are in SI section 5.1. For a lattice with multiple cell types, we replace the scalars C_{ON} , C_{OFF} and K by vectors that are ordered by the cell type. For instance, if we have L cell types, we have $\vec{K} = (K_1, \dots, K_1, K_2, \dots, K_{L-1}, K_L, \dots, K_L)$. Moreover, the interaction terms $f(r_{ij})$ for an interaction matrix $F = \llbracket F_{lm} \rrbracket$ where F_{lm} contains all the interactions terms $f(r_{i \in l, j \in m})$ among cells of type l and

cells of type m . With this notation, we can extend the multicellular Hamiltonian to lattices with an arbitrary number of cell types (Eq. 8). Moreover, we can extend our calculations of P_{ON-ON} and $P_{OFF-OFF}$ to obtain probabilities $P_{ON-ON;l}$ and $P_{OFF-OFF;l}$ that a cell of type l remains in its ON and OFF states, respectively, in the next time step. The total number of trapping configurations is then given by

$$\Omega = \sum_{n=0}^N \sum_{\{p_1, \dots, p_L\}_n} \prod_{l=1}^L P_{ON-ON}^{N_l p_l} P_{OFF-OFF}^{N_l (1-p_l)} \binom{N_l}{N_l p_l} \quad [14]$$

where N_l is the number of cells of type l , p_l is the fraction of cells of type l that are ON, and $\{p_1, \dots, p_L\}_n$ represents all the possible combinations of p_i 's with the constraint that there is a total of n ON-cells on the lattice. This result closely agrees with the exact values obtained for lattices with two cell types.

ACKNOWLEDGMENTS. We thank P. R. Ten Wolde (AMOLF), Y. Blanter (Quantum Nanoscience dept., TU Delft), L. Reese (Bionanoscience dept., TU Delft), A. Raj (Bioengineering dept., Univ. of Pennsylvania), and the members of the Youk group for insightful discussions and/or comments on the manuscript. HY is supported by the European Research Council's Starting Grant (#677972), the Netherlands Organization for Scientific Research (NWO) Vidi award (#680-47-544), and the NWO NanoFront program.

REFERENCES

1. Gregor T, Fujimoto K, Masaki N, Sawai S (2010) The onset of collective behavior in social amoebae. *Science* 328(5981):1021–1025.
2. Sawai S, Thomason PA, Cox EC (2005) An autoregulatory circuit for long-range self-organization in Dictyostelium cell populations. *Nature* 433(7023):323–326.
3. Danino T, Mondragón-Palomino O, Tsimring L, Hasty J (2010) A synchronized quorum of genetic clocks. *Nature* 463(7279):326–330.
4. Liu C, et al. (2011) Sequential establishment of stripe patterns in an expanding cell population. *Science* 334(6053):238–241.
5. Youk H, Lim WA (2014) Secreting and sensing the same molecule allows cells to achieve versatile social behaviors. *Science* 343(6171):1242782–1242782.
6. Doğaner BA, Yan LKQ, Youk H (2015) Autocrine Signaling and Quorum Sensing: Extreme Ends of a Common Spectrum. *Trends Cell Biol.* 26(4): 262–271.
7. Sgro AE, et al. (2015) From intracellular signaling to population oscillations: bridging size- and time-scales in collective behavior. *Mol Syst Biol* 11(1):779–779.
8. Kamino K, et al. (2017) Fold-change detection and scale invariance of cell-cell signaling in social amoeba. *Proc Natl Acad Sci USA* 114(21):E4149–E4157.
9. Antebi YE, Reich-Zeliger S, Hart Y, Mayo A, Eizenberg I (2013) Mapping Differentiation under Mixed Culture Conditions Reveals a Tunable. *PLoS Biol.* 11(7):e1001616.
10. Sporn MB, Todaro GJ (1980) Autocrine secretion and malignant transformation of cells. *N Engl J Med* 303(15):878–880.
11. Maire T, Youk H (2015) Molecular-Level Tuning of Cellular Autonomy Controls the Collective Behaviors of Cell Populations. *Cell Systems* 1(5):349–360.
12. Hart Y, et al. (2014) Paradoxical Signaling by a Secreted Molecule Leads to Homeostasis of Cell Levels. *Cell* 158(5):1022–1032.
13. De Monte S, d'Ovidio F, Danø S, Sørensen PG (2007) Dynamical quorum sensing: Population density encoded in cellular dynamics. *Proc Natl Acad Sci USA*

104(47):18377–18381.

14. Umeda T, Inouye K (2004) Cell sorting by differential cell motility: a model for pattern formation in *Dictyostelium*. *Journal of Theoretical Biology* 226(2):215–224.
15. You L, Cox RS, Weiss R, Arnold FH (2004) Programmed population control by cell-cell communication and regulated killing. *Nature* 428(6985):868–871.
16. Pai A, Tanouchi Y, You L (2012) Optimality and robustness in quorum sensing (QS)-mediated regulation of a costly public good enzyme. *Proc Natl Acad Sci USA* 109(48):19810–19815.
17. Coppey M, Berezhkovskii AM, Sealfon SC, Shvartsman SY (2007) Time and length scales of autocrine signals in three dimensions. *Biophys J* 93(6):1917–1922.
18. Shvartsman SY, Wiley HS, Deen WM (2001) Spatial range of autocrine signaling: modeling and computational analysis. *Biophys J* 81(4):1854–1867.
19. Shvartsman SY, et al. (2002) Autocrine loops with positive feedback enable context-dependent cell signaling. *Am J Physiol, Cell Physiol* 282(3):C545–59.
20. Hoyos E, et al. (2011) Quantitative variation in autocrine signaling and pathway crosstalk in the *Caenorhabditis* vulval network. *Curr Biol* 21(7):527–538.
21. Mehta P, Goyal S, Long T, Bassler BL, Wingreen NS (2009) Information processing and signal integration in bacterial quorum sensing. *Mol Syst Biol* 5:1–11.
22. Cao Y, et al. (2016) Collective Space-Sensing Coordinates Pattern Scaling in Engineered Bacteria. *Cell* 165(3):620–630.
23. Cotterell J, Robert-Moreno A, Sharpe J (2015) A Local, Self-Organizing Reaction-Diffusion Model Can Explain Somite Patterning in Embryos. *Cell Systems* 1(4):257–269.
24. Cotterell J, Sharpe J (2010) An atlas of gene regulatory networks reveals multiple three-gene mechanisms for interpreting morphogen gradients. *Mol Syst Biol* 6:1–14.
25. Ben-Zvi D, Shilo B-Z, Fainsod A, Barkai N (2008) Scaling of the BMP activation gradient in *Xenopus* embryos. *Nature* 453(7199):1205–1211.
26. Haskel-Ittah M, et al. (2012) Self-organized shuttling: generating sharp dorsoventral polarity in the early *Drosophila* embryo. *Cell* 150(5):1016–1028.
27. Graner F, Glazier J (1992) Simulation of biological cell sorting using a two-dimensional extended Potts model. *Phys Rev Lett* 69(13):2013–2016.
28. Vicsek T, Czirók A, Ben-Jacob E, Cohen I, Shochet O (1995) Novel type of phase transition in a system of self-driven particles. *Phys Rev Lett* 75(6):1226–1229.
29. Mora T, et al. (2016) Local equilibrium in bird flocks. *Nat Phys* 12(12):1153–1157.
30. Surkova S, Spirov AV, Gursky VV (2009) Canalization of gene expression and domain shifts in the *Drosophila* blastoderm by dynamical attractors. *PLoS Comp Biol*

5(3):e1000303.

31. Sokolowski TR, Erdmann T, Wolde ten PR (2012) Mutual Repression Enhances the Steepness and Precision of Gene Expression Boundaries. *PLoS Comp Biol* 8(8):e1002654–17.
32. Dubuis JO, Tkačik G, Wieschaus EF, Gregor T, Bialek W (2013) Positional information, in bits. *Proc Natl Acad Sci USA* 110(41):16301–16308.
33. Tkačik G, Gregor T, Bialek W (2008) The Role of Input Noise in Transcriptional Regulation. *PLoS ONE* 3(7):e2774–11.
34. Hillenbrand P, Gerland U, Tkačik G (2016) Beyond the French Flag Model: Exploiting Spatial and Gene Regulatory Interactions for Positional Information. *PLoS ONE* 11(9):e0163628.
35. Erdmann T, Howard M, Wolde ten PR (2009) Role of Spatial Averaging in the Precision of Gene Expression Patterns. *Phys Rev Lett* 103(25):258101–4.
36. Ermentrout GB, Edelstein-Keshet L (1993) Cellular automata approaches to biological modeling. *Journal of Theoretical Biology* 160(1):97–133.
37. Rappaport N, Barkai N (2012) Disentangling signaling gradients generated by equivalent sources. *J Biol Phys* 38(2):267–278.
38. Chen C-C, et al. (2015) Organ-level quorum sensing directs regeneration in hair stem cell populations. *Cell* 161(2):277–290.
39. Walczak AM, Sasai M, Wolynes PG (2005) Self-consistent proteomic field theory of stochastic gene switches. *Biophys J* 88(2):828–850.
40. Acar M, Becskei A, van Oudenaarden A (2005) Enhancement of cellular memory by reducing stochastic transitions. *Nature* 435(7039):228–232.
41. MORAN PAP (1950) Notes on continuous stochastic phenomena. *Biometrika* 37(1-2):17–23.
42. Zwanzig R (2001) *Nonequilibrium statistical mechanics* (Oxford University Press). 1st Ed.
43. Grassberger P (1997) Pruned-enriched Rosenbluth method: Simulations of θ polymers of chain length up to 1 000 000. *Phys Rev E* 56(3):3682–3693.
44. Hopfield JJ (1982) Neural networks and physical systems with emergent collective computational abilities. *Proc Natl Acad Sci USA* 79(8):2554–2558.
45. Amit D, Gutfreund H, Sompolinsky H (1985) Storing infinite numbers of patterns in a spin-glass model of neural networks. *Phys Rev Lett* 55(14):1530–1533.
46. Kirkpatrick S, Sherrington D (1975) Solvable model of a spin-glass. *Phys. Rev. Lett.* 35(26):1792–1796.
47. Bonilla LL, Padilla FG, Parisi G (1996) Analytical solution of the Monte Carlo dynamics of

- a simple spin-glass model. *Europhys Lett* 34(3):159-164.
48. Walczak AM, Wolynes PG (2009) Gene-gene cooperativity in small networks. *Biophys J* 96(11):4525–4541.
 49. Sagués F, Sancho JM, García-Ojalvo J (2007) Spatiotemporal order out of noise. *Rev Mod Phys.* 79:829-882.
 50. Sancristóbal B, Rebollo B, Boada P, Sanchez-Vives MV, Garcia-Ojalvo J (2016) Collective stochastic coherence in recurrent neuronal networks. *Nat Phys* 12(9):881–887.
 51. García-Ojalvo J (2011) Physical approaches to the dynamics of genetic circuits: a tutorial. *Contemporary Physics* 52(5):439–464.
 52. Raj A, van Oudenaarden A (2008) Nature, nurture, or chance: stochastic gene expression and its consequences. *Cell.* 135:216-226.
 53. Tkačik G, Walczak AM (2011) Information transmission in genetic regulatory networks: a review. *J Phys Condens Matter* 23(15):153102.
 54. Friedlander T, Prizak R, Guet CC, Barton NH, Tkačik G (2016) Intrinsic limits to gene regulation by global crosstalk. *Nat Commun* 7:12307.
 55. Thattai M, van Oudenaarden A (2001) Intrinsic noise in gene regulatory networks. *Proc Natl Acad Sci USA* 98(15):8614–8619.
 56. Tkačik G, Dubuis JO, Petkova MD, Gregor T (2015) Positional information, positional error, and readout precision in morphogenesis: a mathematical framework. *Genetics* 199(1):39–59.
 57. Sanchez A, Golding I (2013) Genetic determinants and cellular constraints in noisy gene expression. *Science* 342(6163):1188–1193.
 58. Xu H, Skinner SO, Sokac AM, Golding I (2016) Stochastic Kinetics of Nascent RNA. *Phys Rev Lett* 117(12). doi:10.1103/PhysRevLett.117.128101.
 59. Cheong R, Rhee A, Wang CJ, Nemenman I, Levchenko A (2011) Information Transduction Capacity of Noisy Biochemical Signaling Networks. *Science* 334(6054):354–358.
 60. Alberts B, et al. (2014) *Molecular Biology of the Cell* (Garland Science). 6 Ed.
 61. Combs PA, Eisen MB (2013) Sequencing mRNA from cryo-sliced Drosophila embryos to determine genome-wide spatial patterns of gene expression. *PLoS ONE* 8(8):e71820.
 62. Junker JP, et al. (2014) Genome-wide RNA Tomography in the zebrafish embryo. *Cell* 159(3):662–675.
 63. Mallavarapu A, Thomson M, Ullian B, Gunawardena J (2009) Programming with models: modularity and abstraction provide powerful capabilities for systems biology. *Journal of The Royal Society Interface* 6(32):257–270.

Figure captions:

Fig. 1. Behavioural phases of secrete-and-sense cells.

(A) Example of secrete-and-sense cells' disorder-to-order dynamics simulated by a cellular automaton. The top layer shows a steady state spatial pattern formed by ON-cells (black circles) and OFF-cells (white circles).

(B) Phase diagrams denoting all possible behavioural phases of secrete-and-sense cells. Each colour represents a unique phase. Coloured lines represent phase boundaries that shift as the interaction strength is tuned. Insulating phases (orange, blue, yellow) allow only self-interaction while conducting phases (green, brown, white) allow cells to exchange information through their common signal such as ON-cell (black circle) activating an OFF-cell (white circle) into an ON-cell at the next time step (in the activate-phase). Black arrows represent interactions. Red arrows represent a flow in time. Phase diagram of the secrete-and-sense cells that operate with (top) a weak cell-cell interaction strength ($f(N, a_0) = 0.518$; $a_0 = 1.5$), (middle) a nearly critical cell-cell interaction strength ($f(N, a_0) = 0.967$; $a_0 = 1.0$), and (bottom) with a strong cell-cell interaction strength ($f(N, a_0) = 2.302$; $a_0 = 0.5$).

Fig. 2. Macrostates of secrete-and-sense cells - Cellular lattices act as particles that drift and diffuse.

(A) A macrostate (p, I) of cellular lattice (right column) is an ensemble of microstates (i.e., individual configurations) of cellular lattice that have the same p and I . p = fraction of population that are ON-cells; I = spatial order parameter ($0 \leq |I| \leq 1$).

(B) (Left column) Probability density maps showing $p(t_{final})$ - the steady state value of p when the cellular automaton terminates at time t_{final} - as a function of $p(t=0)$, which is the initial value that the automaton starts with. For each value of $p(t=0)$, we ran at least 1000 cellular automata, each with the same parameters but with a different, completely disordered microstate ($I \approx 0$) that we randomly chose. Each coloured "pixel" here represents a probability (see colour bar at the bottom). White regions represent values near zero probability. Dashed red and green lines are slices along the density maps that correspond to the trajectories in the right column. (Right column) Macrostate trajectories ($p(t), I(t)$) as a function time t . For each phase, 30 trajectories that start with the same macrostate are shown (red curves). Arrows represent general directions

of flow in each trajectory. Insets in each panel show zoomed-in views of a few trajectories. Black dots in the insets represent termination of trajectories. In each of the three conducting phases, all 30 trajectories start with the same initial values of p and I - Activate phase: $p(t=0)=0.2$ (with $K=14$, $C_{ON}=16$); deactivate phase: $p(t=0)=0.8$ (with $K=18$, $C_{ON}=7$); activate-deactivate phase: $p(t=0)=0.5$ for red trajectories and $p(t=0)=0.8$ for green trajectories (with $K=16$, $C_{ON}=8$). For all three phases, $N=121$ and $R=0.2a_0$.

(C) (Left column) Probability density maps obtained as in (b). (Right column) With the same parameters as in the left column, probability density maps obtained by Monte Carlo simulations based on our theory of drifting-and-diffusing particles (with analytical estimates of key probability distributions) and our "branching algorithm" (see SI sections 2.3 and 2.4). Activate phase: $K=20$, $C_{ON}=15$, $a_0=1.5$; deactivate phase: $K=6$, $C_{ON}=15$, $a_0=1.5$; autonomy phase: $K=12$, $C_{ON}=15$, $a_0=1.5$; Activate-deactivate phase: $K=15$, $C_{ON}=8$, $a_0=0.5$. In all phases, $N=225$ and $R=0.2a_0$.

(D) Average number $\langle t_{final} \rangle$ of time steps taken by the secrete-and-sense cells to reach steady-state configurations as a function of the initial value of p , $p_{initial}$. Each black data point is an average over at least 1000 cellular automata for each value of $p_{initial}$. Red curves are analytical estimates based on our theory of drifting-and-diffusing particles in phase space.

Fig. 3. Cellular lattices act as particles that drift and diffuse downwards on pseudo-energy landscapes where they can be trapped.

(A) Example of the polygonal analysis, with polygon- v , for studying disorder-to-order transition. L_v and A_v are the number of edges and the number of enclosed ON-cells for polygon- v .

(B) Comparing the analytical formula for $I(t)$ (Eq. 4 - black curve) obtained by the polygonal analysis shown in (a) with the exact value of $I(t)$ obtained from a cellular automaton ($N=121$, $a_0=0.5$, $R=0.2a_0$, $K=10$, $C_{ON}=5$).

(C) Pseudo-energy landscape obtained by plotting $h(p, I) = H/N$ - multicellular Hamiltonian H divided by N . $N=121$, $a_0=0.5$, $R = 0.2a_0$, $K=16$, $C_{ON}=8$. Particle (orange circle), representing a cellular lattice, rolls down the landscape.

(D) (Left column) Each phase shows 100 particle trajectories (red and blue curves), some of which appeared in Fig. 2B, with the same parameters as in Fig. 2B but now with the pseudo-energy landscapes in the backgrounds (heat maps). Arrows indicate general directions of the particle flows over time. Black curves indicate theoretically predicted maximum possible value of I as a function of p (see SI section 3.2). (Right column) Normalized Hamiltonian ($h = H/N$) for each trajectory in the left column. All are for $N=121$ cells.

(E) (Top) Same parameters as the activate-deactivate phase in (d) but now with more cells ($N=2500$). Red trajectories start with $p=0.4$, brown trajectories start with $p=0.5$, and blue trajectories start with $p=0.6$. Black curve indicates theoretically predicted maximum possible value of I as a function of p . (Bottom) Normalized Hamiltonian ($h = H/N$) for each brown trajectory in top panel.

(F) Pseudo-energy landscapes for three different regimes of the signal field B in and that boundaries of the activate-deactivate phase: (Top left) At a boundary between activate and deactivate phases ($B=2.6$, $K=7.3$, $C_{ON}=5$), (Top right) Within activate-deactivate phase ($B=0$, $K=9.9$, $C_{ON}=5$), (Bottom right) At a boundary between deactivate and activate-deactivate phases ($B=-2.6$, $K=12.5$, $C_{ON}=5$). (Bottom left) Corresponding phase diagram denoting signs of B . In all cases, $N=225$, $a_0=0.5$, $R=0.2a_0$.

Fig. 4. Stochastic sensing – Noise liberates trapped particles and push them into new trapping configurations with higher spatial orders.

(A) Schematics of noisy secrete-and-sense cells. Each cell can have a different activation threshold $K + \delta K$, where δK is a Gaussian noise with a zero mean and variance α^2 .

(B) Examples of p , I , and $h (=H/N)$ for low noise ($\alpha = 0.2$) and high noise ($\alpha = 0.5$). In both cases, $N=121$, $R=0.2a_0$, $a_0=0.5$, $K=16$, and $C_{ON}=8$ (corresponds to activate-deactivate phase). In this case, theoretically predicted minimum value of α required for perturbing a lattice configuration that is a steady-state of the deterministic automaton is 0.4 (see SI section 4.2).

(C) Example of noise-driven disorder-to-order transition an activate-deactivate phase ($K=10$, $C_{ON}=5$) with $p(t=0)=0.50$. Black circles are ON-cells and white circles are OFF-cells. Noise strength $\xi=0.5$, $N=441$, $a_0=0.5$, and $R=0.2a_0$. Zoomed-in (grey boxes) drift-diffusion dynamics, occurring on slow time scales.

(D) Comparing the deterministic secrete-and-sense cells (left column) and the noisy stochastic secrete-and-sense cells (right column) with the same parameter values in the activate-deactivate phase ($N=441$, $R=0.2a_0$, $a_0=0.5$, $K=10$, $C_{ON}=5$, and noise strength $\xi=0.1$). 100 trajectories (red curves), each starting at $p=0.5$ and $I \approx 0$, shown for both types of cells. Black dots indicate terminal points of each trajectory. Dashed black curve is the theoretically predicted maximum value of I as a function of p (same as in Fig. 3). Dashed orange curve is the theoretically predicted maximum value of I as a function of p when noise-driven ordering is present (formula in SI section 4.5).

(E) Average number $\langle t_{final} \rangle$ of time steps taken by the noisy secrete-and-sense cells to form steady-state configurations a function of the initial value of p , $p_{initial}$. Each black data point is an average over at least 1000 cellular automata for each value of $p_{initial}$. Red curves are analytical estimates based on our theory of drifting-and-diffusing particles with noisy sensing.

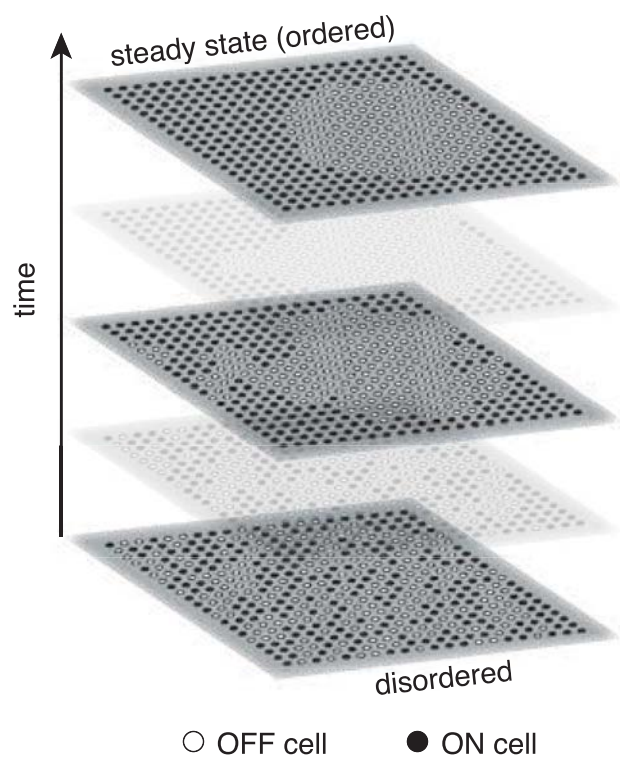
Fig. 5. Extension to lattices with any number of cell types and signalling molecules.

(A) Examples of secrete-and-sensing and paracrine signalling. L types of cells with M types of signalling molecules.

(B) Examples of triangular lattices with two types ($L=2$) of secrete-and-sense cells (circles and rectangles) that share the same signalling molecule ($M=1$). For each lattice, $N=400$ cells, $a_0=0.5$, $R=0.2$, and $f_N=2.358$. Using the formalism detailed in SI section 5.1, we obtain interaction strength f_{lm} between cell type l and cell type m : (top left) - $f_{11} = 0.854$, $f_{12} = 0.325$, $f_{22} = 0.854$; (top right) - $f_{11} = 0.142$, $f_{12} = 0.447$, $f_{22} = 1.321$; (bottom left) - $f_{11} = 0.147$, $f_{12} = 0.443$, $f_{22} = 1.326$; (bottom right) - $f_{11} = 0.585$, $f_{12} = 0.594$, $f_{22} = 0.585$.

(C) Fraction p_1 of cells of type 1 that are ON (blue curves) and fraction p_2 of cells of type 2 that are ON (red curves) obtained through cellular automata for two types of secrete-and-sense cells with shared signal ($L=2$, $M=1$, $N=400$, $N_1=120$, $N_2=280$, $a_0=0.5$, $R_1=R_2=0.2a_0$, $C_{ON,1}=8$, and $C_{ON,2}=5$). All start with $p_1=p_2=0.5$. B_u is the signal field for cell type u ($u=1, 2$). The signs of B_u determine cell type k 's change in p_u over time. If neither B_1 nor B_2 is zero, then p_u increases over time if $B_u > 0$ and decreases over time if $B_u < 0$. When $B_u \approx 0$, then p_u nearly stays the same for the first several time steps and then follows the direction of change of the other cell type's p .

A



B

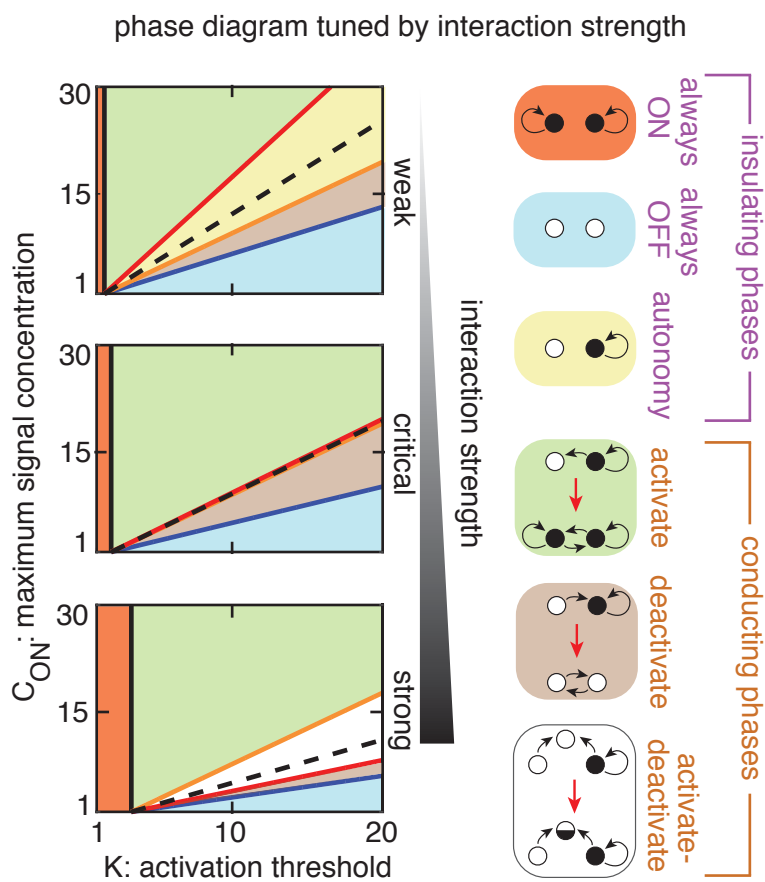


Fig. 1

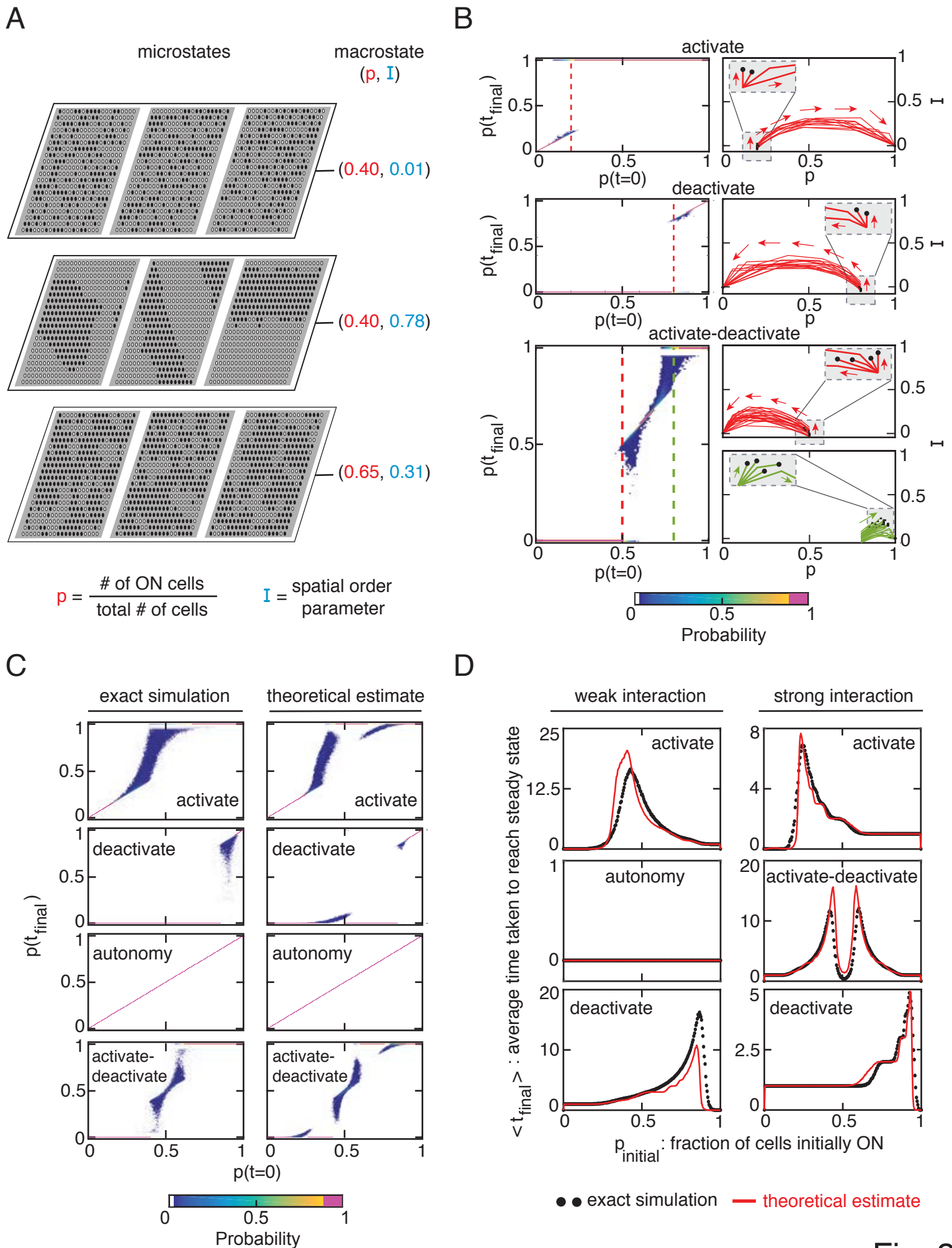


Fig. 2

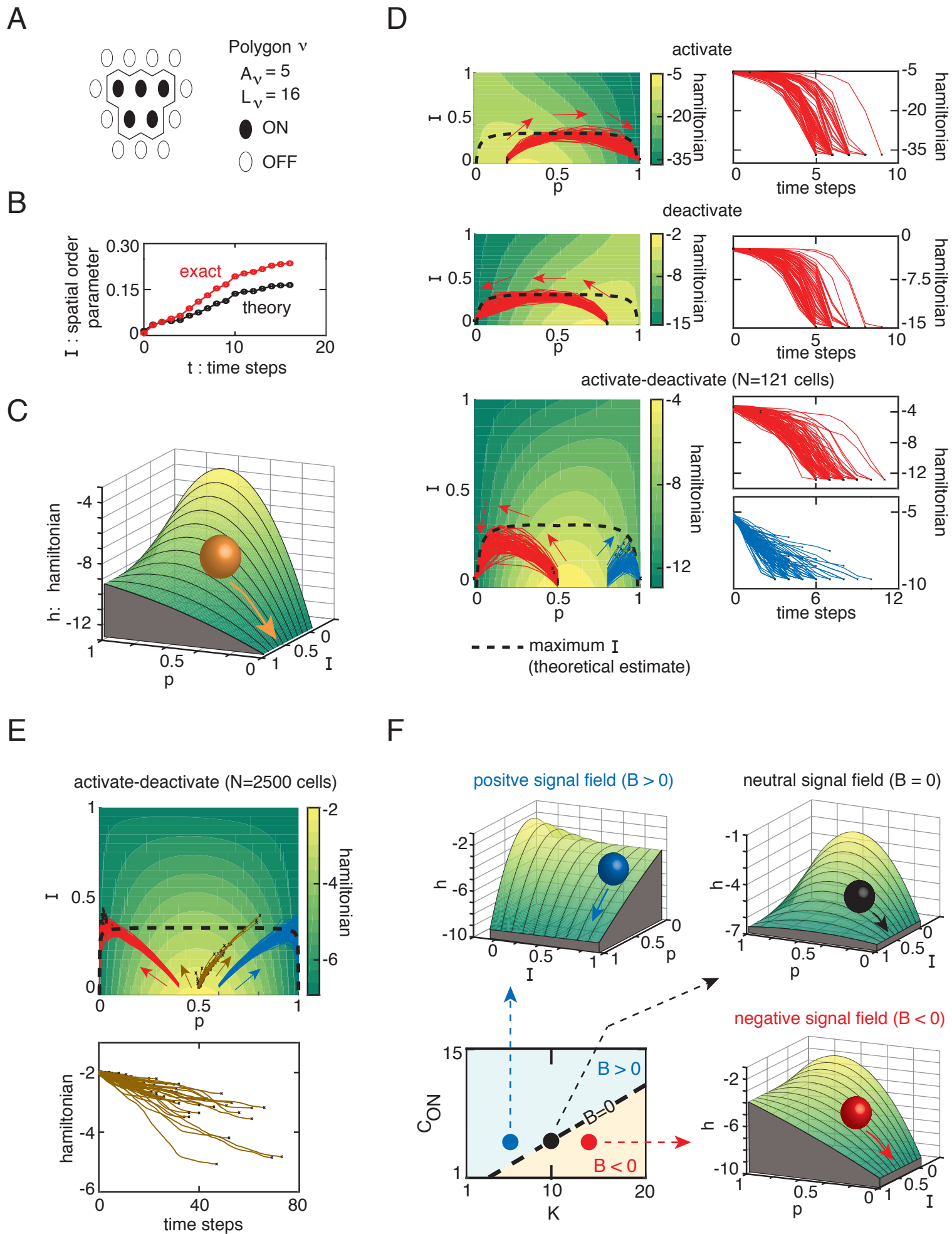
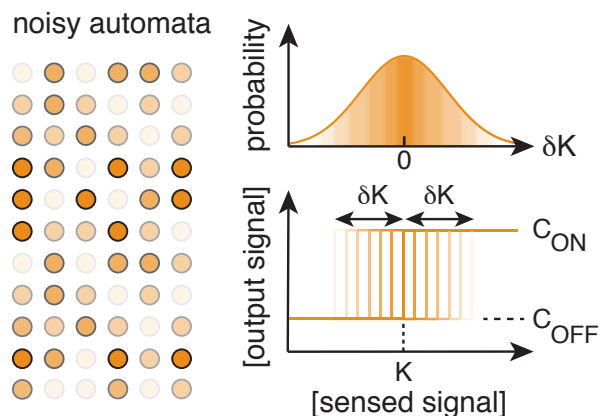
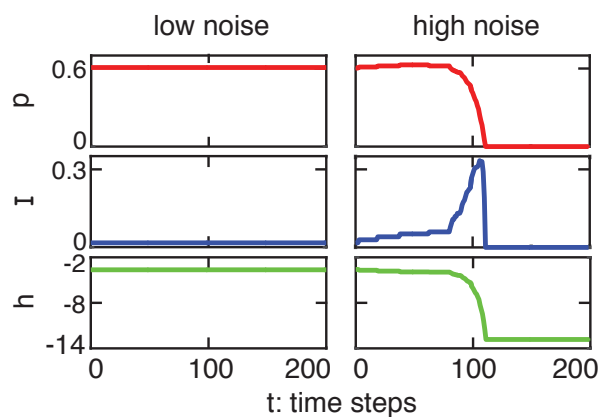


Fig. 3

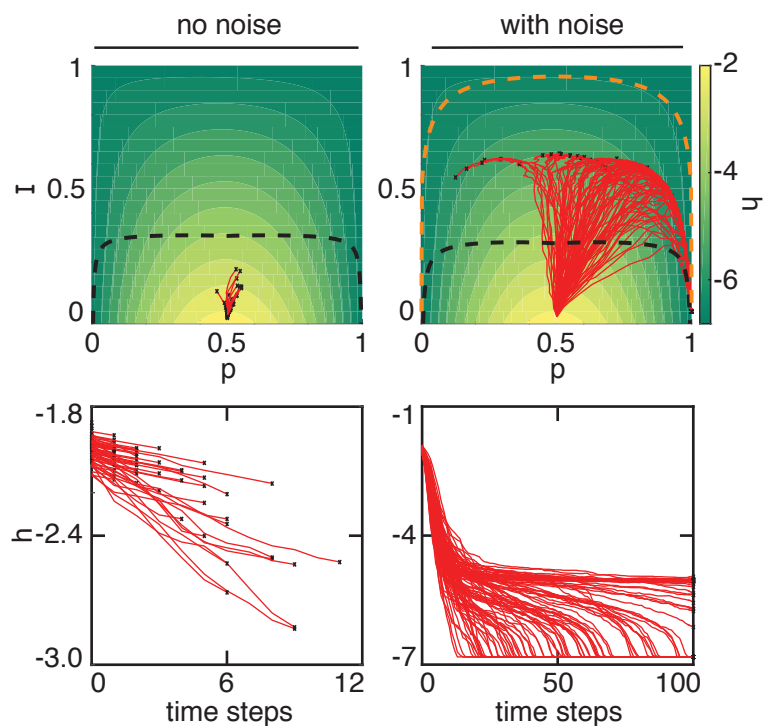
A



B



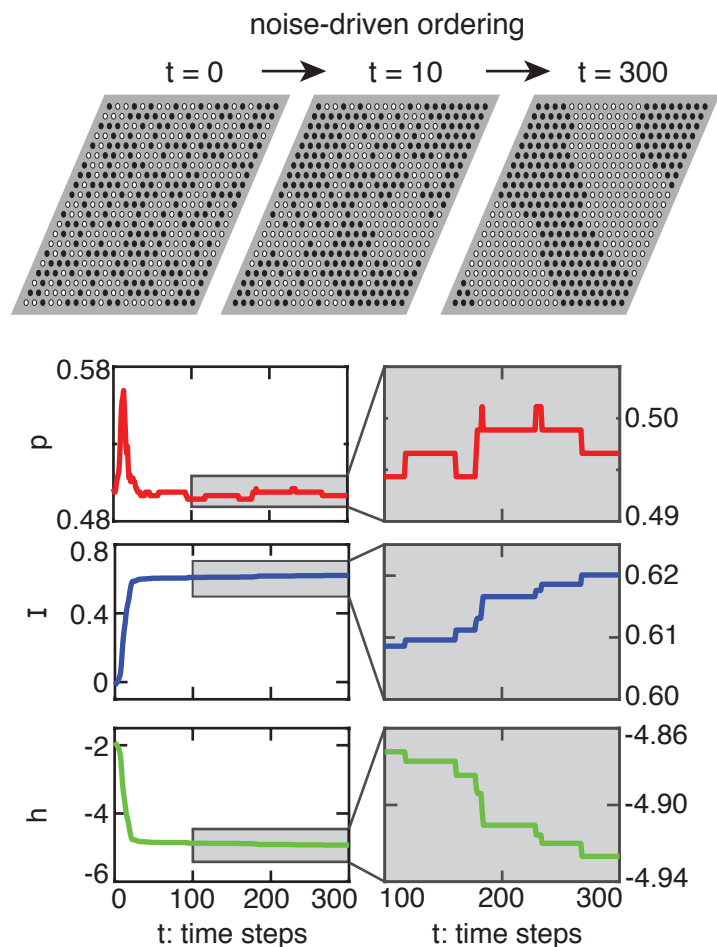
D



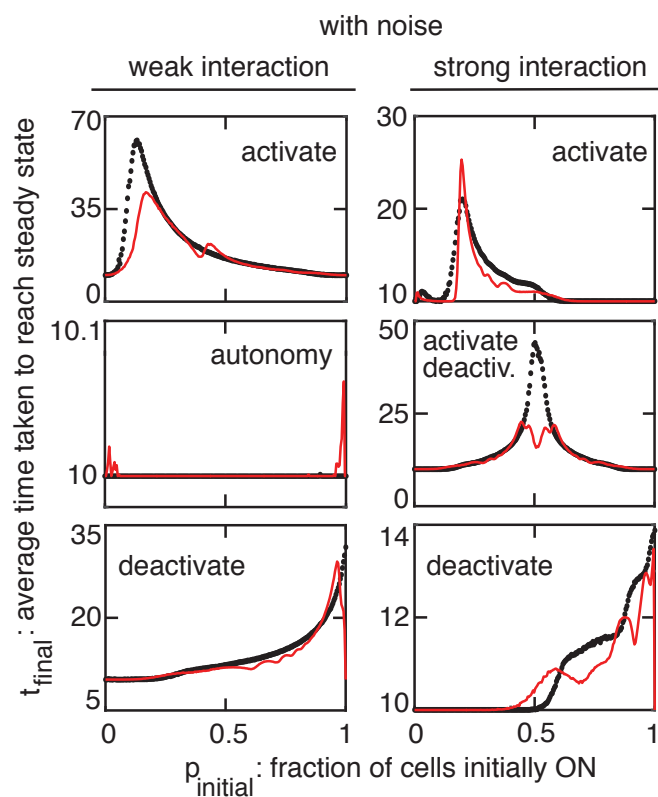
--- maximum I (without noise)

--- maximum I (with noise-driven ordering)

C



E

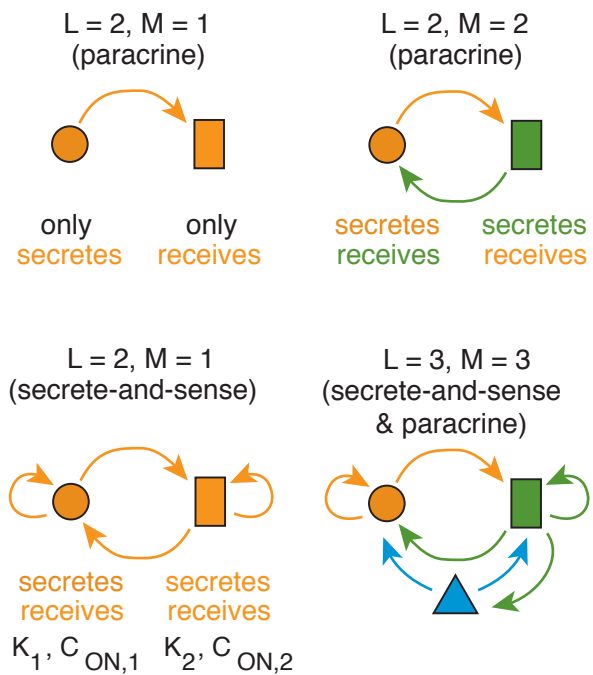


●● exact simulation — theoretical estimate

Fig. 4

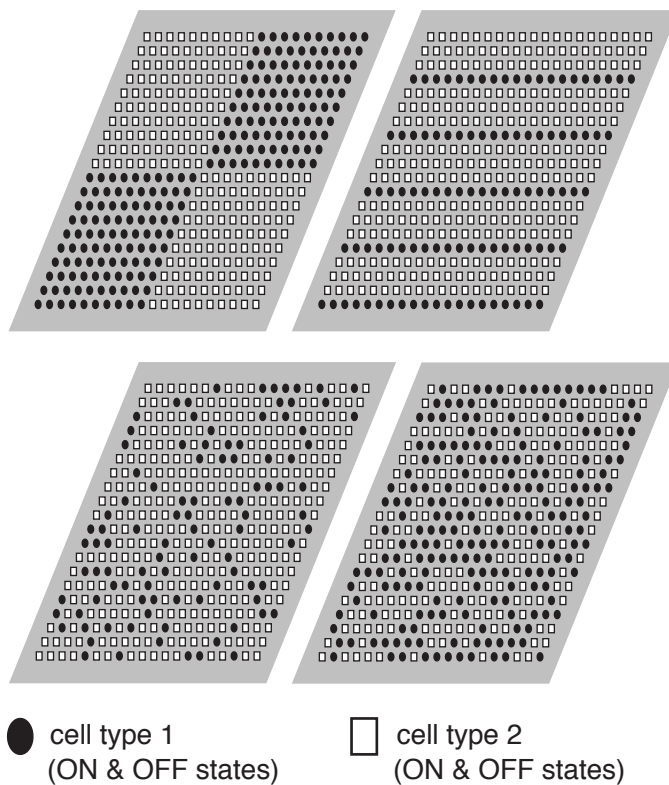
A

L cell types, M signalling molecules



B

L = 2, M = 1



C

L = 2, M = 1 (secrete-and-sense cells)

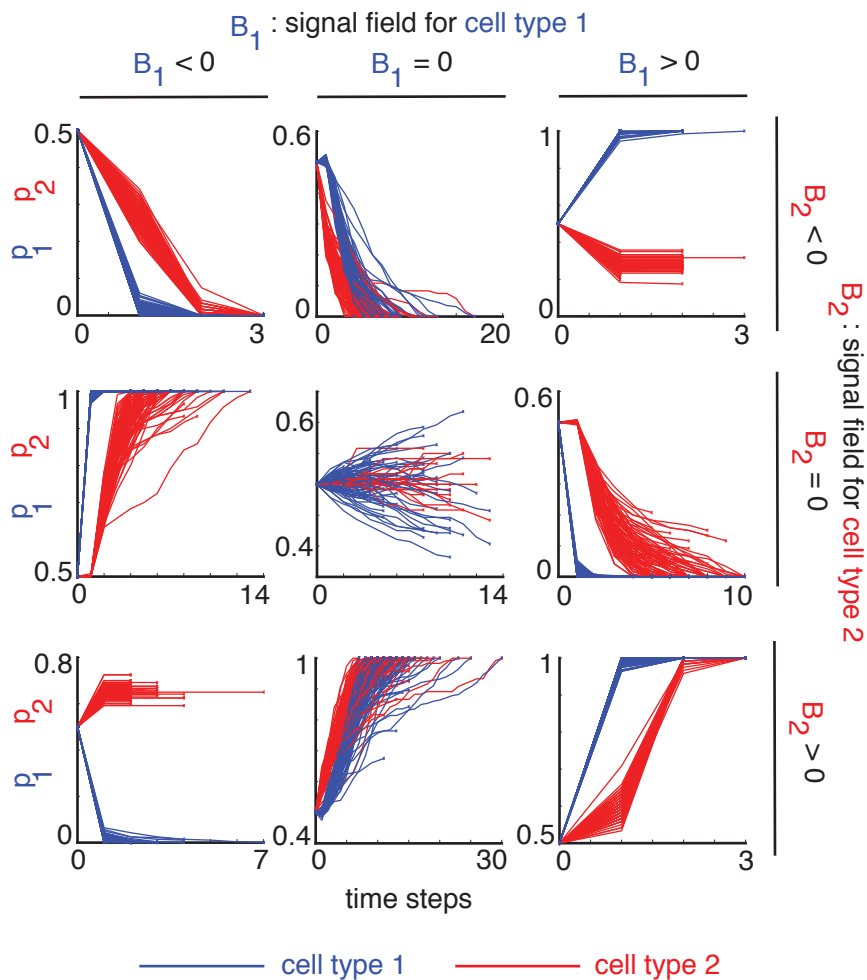


Fig. 5